International Journal of Environmental Sciences
ISSN: 2229-7359
Vol. 11 No. 23s, 2025
https://theaspd.com/index.php

Optical and Radiation Shielding Studies on Borobismuth Iron Oxide-Samarium Bismuth Titanate Glass-Matrix Samples

Aafreen Sultana[1], T.sravan Rao[2], B. Srinivas[2], G. Ramadevudu[2], Md.Shareefuddin[1] G. Ramadevudu[2] and N.V. Prasad[1*]
[1]Material research laboratory, Department of Physics, Osmania University, Hyderabad.
[2]Department of Physics, Vasavi college of Engineering, Ibrahimbagh, Hyderabad
***Corresponding author email id: nvp1969@rediffmail.com**

Abstract

Glass matrix with the chosen composition (100-x) [0.7Bi_2O_3-0.2B_2O_3-0.1Fe_2O_3] + x ($Bi_{3.75}Sm_{0.75}Ti_3O_{12}$) (with x=30, 40, 50, 60 wt.%), were prepared by conventional melt –quench method. The XRD pattern shows the dominant phase of crystalline nature, over the amorphous nature. UV-visible spectra for all the glass-matrix samples were taken in the range of 200-900 nm. Optical parameters like energy gaps (E_{gap}), refractive index, molar polarizability, metallization criterion etc were calculated. Oxygen packing density was found to decrease with increasing the $Bi_{3.75}Sm_{0.75}Ti_3O_{12}$ (BST) content, and hence BST acts like a glass network modifier. Raman spectra results conformed the layered-perovskite structure with distorted TiO_6 octahedral, which is considered to be the characteristic feature for layered-structure glass ceramics. Polaron radius of the samples increased from 9.74 to 14.1 Å, with increasing the BST composition in the glass-matrix. FTIR Spectroscopic results have shown the presence of tri, tetra, penta borate units with distorted BiO_6 units. Optical spectroscopic measurements were carried out on samples and the insights prove that the optical band gap got narrowed down from (1.73eV-1.48 eV). From this one can presume to create a room for photovoltaic applications. Gamma radiation shielding properties were studied using PhyX/PSD software. MAC (Mass Attenuation Coefficient) values were found to be high in the energy range of 0.01MeV- 0.04MeV. The effective atomic number (Z_{eff}), electron density (N_e), mean free path (MFP) and half-value layer (HVL) values were evaluated for all the compositions. The gamma radiation studies on glass-matrix exhibit excellent gamma ray shielding features and therefore these materials are considered to be future environment-friendly nuclear shielding materials.

1. INTRODUCTION

Structurally stable, glass- ferroelectric materials are evolving as a promising and intensely probed candidates due to their unique properties like glass-ceramic mixed nature, high mechanical strength, high dielectric constant, and their remarkable gamma radiation properties thereby paving their way in the diverse fields of technological applications in the field of optoelectronics and radiation shielding field [1-4]. The glass-matrix ferroelectric materials act as a good host for doping of rare earth elements enhancing their electrical properties as a result of positive structural changes [5]. Literature survey reveals that rare earth-based glasses embedded with ferroelectric material have a blend of interesting and novel structural, optical, electrical properties [6-10]. Non-transparent glass materials are being used to protect from gamma ray radiation. Gamma ray tradition is absorbed by glass materials and acts as shielding. In addition, bismuth-based glasses, known to be lead-free, play a significant role in the shielding of intense radiation. Many high metal-oxide doped glasses are found to be useful to protect radiation, preferable for high energy radiation shielding [11,12].

Aurivillius-based layered-perovskites are a family of bismuth layered structure ferroelectrics, with the general formula $[Bi_2O_2]^{2+}[A_{n-1}B_nO_{3n+1}]^{2-}$. Where A and B represent bismuth and titanium ions. It is reported that Sm modified three-layered compound ($Bi_4Ti_3O_{12}$) consists of three-perovskite units of $(Bi_2Ti_3O_{10})^{2-}$ in a alternating $(Bi_2O_2)^{2-}$ layers. These materials offer wide range of optical properties including UV-Visible absorption and tunable band structure [11]. These materials are suitable for solar energy applications. The unique electronic structure of Bi^{3+} is consist of $6s^2$ lone pairs and oxygen p-orbitals. This leads to a lowered band gap energy and improved visible-light absorption, making them effective photocatalysts for water splitting and pollutant degradation [12].

Samarium (Sm) doped BIT ($Bi_{3.25}Sm_{0.75}Ti_3O_{12}$; BST) has shown high dielectric constant, remanent polarization and lower transition temperature, compared to the parent compound ($Bi_4Ti_3O_{12}$, BIT) [13]. On the other hand, rare earth modified BIT compounds have shown reduced leakage-currents and therefore these materials are used in integrated optoelectronic devices [14]. The glass matrix Fe_2O_3-Bi_2O_3-

B_2O_3 system can be engineered to form glass-ceramics with a magnetic and dielectric phase. These materials are showcasing of both magnetic and dielectric phases [15].

The presence of transition metal oxides with addition of Bi_2O_3 have shown new possibilities due to the presence of different valence states of Fe/Ti ions. The addition of Fe_2O_3 in the glass matrix enhances the chemical durability and their stability. Keeping in the view the effect of transition metal ions in modifying the glass-ceramic structure and their wide range of applications, it is of interest to carry out the detailed study of the effect of rare earth modified BIT on Fe_2O_3-Bi_2O_3-B_2O_3 glass matrix. It is a known fact that the high atomic number is found to be more favourable to ecological profile. Therefore, these materials are future promising alternative lead-free for photoelectric absorption.

In the present investigation, the motivation of ferroelectric phase on the Fe_2O_3-Bi_2O_3-B_2O_3 glass-matrix. A detailed optical, FTIR, Raman and gamma radiation shielding parameters were calculated. Such systematic studies were nor reported so far.

2. Experimental procedure

Glass composition of (100-x) [$0.7Bi_2O_3$-$0.2B_2O_3$-$0.1Fe_2O_3$] + x ($Bi_{3.75}Sm_{0.75}Ti_3O_{12}$), with x=30, 40, 50, 60 wt.%, by weight, were fabricated using the conventional melt – quench techniques. Initially the BST composite was prepared by taking (Bi_2O_3) (> 99.9% purity), Sm_2O_3 (>99.9% purity) and (TiO_2) (>99% purity) powders in the required stoichiometric ratio and mixed thoroughly. The powders were hand grinded using mortar and pestle for 8 hrs. Additionally ball milled with ethanol for 12 hrs. and was dried under the IR lamp. Furthermore, the powder was poured in the porcelain crucible and sintered in the microprocessor based programmable furnace between temperature of 500^0C-850^0C at the rate of 5^0/min. The sintered powder was again hand grinded in agate mortar for 4hrs and the X-ray diffractogram was obtained on the samples. Finally, the chosen composition of (100-x) [$0.7Bi_2O_3$-$0.2B_2O_3$-$0.1Fe_2O_3$] + x ($Bi_{3.75}Sm_{0.75}Ti_3O_{12}$), where x=30, 40, 50, 60 wt.%. With proportionate amounts of Bi_2O_3, B_2O_3, Fe_2O_3 and BST powders were properly mixed and heated in the furnace at 1200 – 1250^0C for half an hour in a non-reactive porcelain crucibles with lid and the molten viscous fluid was being swirled at the intermediate stages to ensure the homogeneity of the fluid and then was quickly quenched by pouring it onto the preheated stainless steel plate (maintained at nearly 100^0 C) with the help of another plate. The prepared glass-matrix samples were kept in the porcelain crucibles with lid covered for half an hour to hinder the surface oxidation in the sample and to get the homogeneity in the structure. The prepared glass-matrix and their codes were given in Table 1.

S.NO.	x BST (wt. %) ($Bi_{3.25}Sm_{0.75}Ti_3O_{12}$)	(100-x) BBF [wt.%] ($0.7Bi_2O_3$-$0.2B_2O_3$-$0.1Fe_2O_3$)	Sample code
1.	30	70	BST30 -BBF70
2.	40	60	BST40 - BBF60
3.	50	50	BST50 - BBF50
4.	60	40	BST60 - BBF40

Table :1 Sample code of the prepared samples

X-ray diffraction patterns were recorded on the glass-matrix samples, using Pan Analytic X'pert plus diffractometer, with Cu-kα (1.54 Å) radiation. The density of the samples was measured using the Archimedes principle using xylene as a liquid medium. Scanning electron microscope images and elemental analysis were obtained with electron dispersive spectroscopy, which is attached to ZEISSEVO18 microscope. Fourier transformation infrared (FTIR) spectra were recorded using FTIR-8400S spectrophotometer. Optical absorption studies were with the help of UV-VIS 3092 spectrometer. Raman spectra were recorded with the help of Horiba Jobin Yvon Raman spectrometer. The wavelength of laser source is 785 nm. The theoretical-studies of gamma radiation on these materials were obtained using Phy-X program. Based on the computer simulated software, different simulated parameters were calculated at a given energy value. The parameters like effective mass number (Z_{eff}) mean free path (MFP), linear attenuation coefficient (LAC) and mass attenuation coefficient (MAC) were calculated in the photon energy range (0.015eV-15Mev).

3. RESULTS AND DISCUSSIONS

Fig 1 shows the XRD pattern of all x BST+(100-x) BBF, where x = 30,40,50 and 60 in the range of $10^0 \leq \Theta \leq 80^0$.

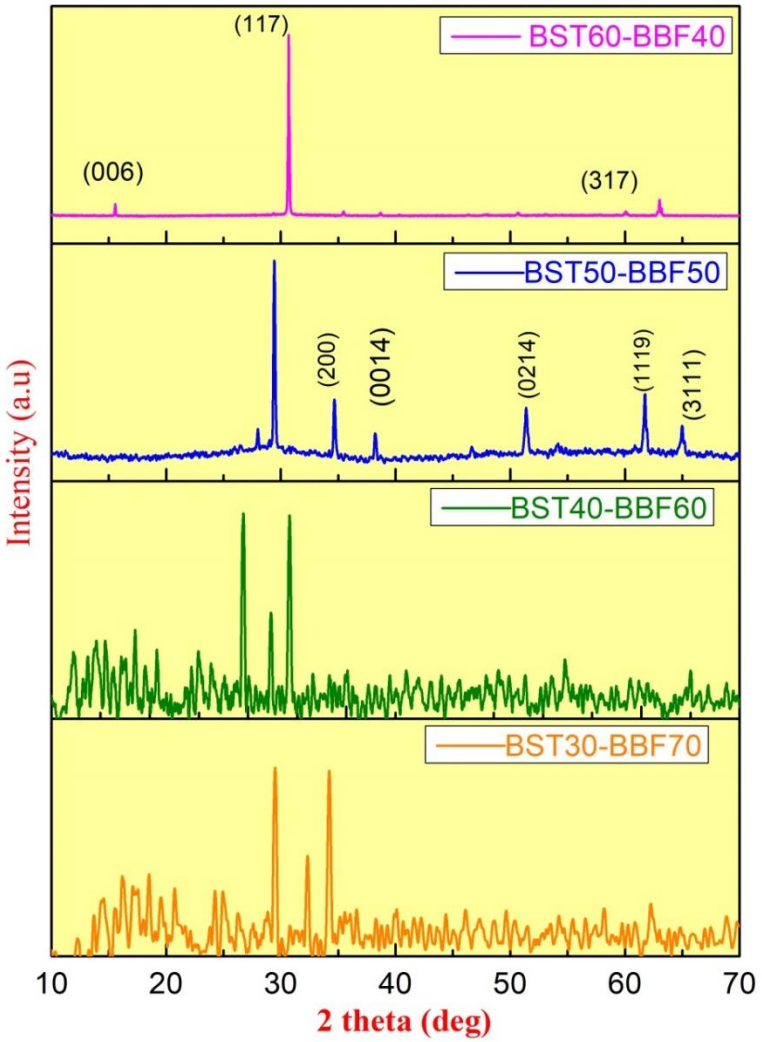

Fig 1. XRD pattern of the all glass-matrix samples

It is clear from the observed XRD pattern that the BST content is responsible for the crystallinity of the sample. The sharp Bragg peaks around 30^0 of 2 is found to merge into single peak. The corresponding high intense plane (117) confirms the single phase of BST60-BBF40. This could be due to the successful replacement of Sm^{+3} ions with Bi^{+3} ions in the layered-perovskite compound. Only one sharp peak observed for high concertation BST indicates the presence of partial-crystalline nature of layered-perovskite namely BST. The absence of well-defined peaks of BST ceramic confirms the less crystalline or partial glassy nature of the material. This indicates the existence of short-range order of atomic arrangements with long-range order.

Density of the glass-matrix were calculated from the Archimedes Principle using the following relation:

$$\rho = \frac{W_a}{W_a - W_b} * \rho_b \qquad (1)$$

Where ρ_b is the density of the reference liquid (xylene=0.865 g/cc) and W_a, W_b is the weight of the glass-ceramic samples measured in air and xylene respectively.

Molar volume, transition metal ion concentration, polaron radius and Interionic distance has been computed through the relations given below [16]:

S. No	Parameter	Formula
1	Molar Volume (Vm)	$V_m = \frac{M_c}{\rho}$
2	Transition metal ion concentration (N)	$N = \frac{0.01 * N_a * \rho}{V_m}$
3	r_p (Polaron radius)	$r_p = \left(\frac{1}{N}\right)^{1/3}$
4	Interionic distance (r_i)	$r_i = \frac{1}{2}(\pi/6N)^{\frac{1}{3}}$

Table 2: The mathematical relations for the physical parameters

Here M_C is the molecular weight of the sample, N_A is Avogadro number, ρ is density and V_m are molar volume of the samples respectively. The parameters calculated from the relations given in Table2, were summarized in the Table 3.

S.no	Sample Code	Density (gm/cc)	Molar Volume (cc/mol)	Transition metal ion concentration (N_i) /cc x 10^{20}	Polaron radius (r_p) (Å)	Interionic distance (r_i) (Å)	Oxygen Packing Density (OPD) g. atm/L	E_{opt} (eV)	Urbach energy (eV)
1	BST30 - BBF70	6.48	87.18	4.4	9.74	5.29	240.88	1.74	0.101
2	BST40 - BBF60	6.81	92.67	4.42	13.1	5.28	226.61	1.46	0.06
3	BST50 - BBF50	6.61	105.55	3.77	13.8	5.57	199.95	1.48	0.05
4	BST60 - BBF40	6.75	113.145	3.59	14.1	5.67	185.6	1.48	0.06

Table 3. Physical parameters of x BST+(100-x) BBF, where x = 30,40,50 and 60

It can be seen from Table 3, that the density values rise with increase in BST concentration and so did the molar volume. This increasing nature of the molar volume is attributed to the conversion of bridging oxygen (BO) to non- bridging oxygen atoms (NBO) in the glass matrix, due to the rise in crystallinity with BST. The same could be due to the increase of bismuth atoms in proportion with other elements in the samples. From the XRD patterns the additional peaks observed for low concentration BST could be attributed to the presence of mixed phases. Similar observations were seen in the intergrowth compounds where two mixed phases exist. Multiple XRD peaks also indicates that crystalline materials have formed within the glass matrix. The additional XRD peaks observed around 30° of 2θ directly related to the glass's chemical composition and the heat treatment protocol, particularly the sintering temperature. Different compositions and sintering temperatures promote the formation of different crystalline planes and influence their size and distribution. It should be remembered here that the bismuth oxide characteristic peaks appear at 28° and 56° of 2θ Bragg angle. The broad XRD peaks observed for low concentration of BST is considered to be the characteristic peaks of bismuth oxide or boro-bismuth oxide amorphous (glass) nature.

The optical absorbance spectroscopy in UV-visible (200nm-800nm) region for different BST concentrations embedded in BBF glass-matrix, as shown in the Fig 2. From absorption plot,a dispersion is seen between low BST and high concentrations, as encircled in the plot. This could be due to the conversion of glass nature to mixed glass-crystalline nature of the sample. The dispersion peak observed at 350 nm is attributed to the presence of Bi^3 ion and the intensity of the peak position is more or less depend upon the BST content in the matrix. It is reported in the literature that Bi-doped glasses show a broad absorption peak at around 350 nm and being considered to be the characteristic of the $1S_0 \rightarrow {}^3P_1$ electronic transition of the bismuth ions [17].

International Journal of Environmental Sciences
ISSN: 2229-7359
Vol. 11 No. 23s, 2025
https://theaspd.com/index.php

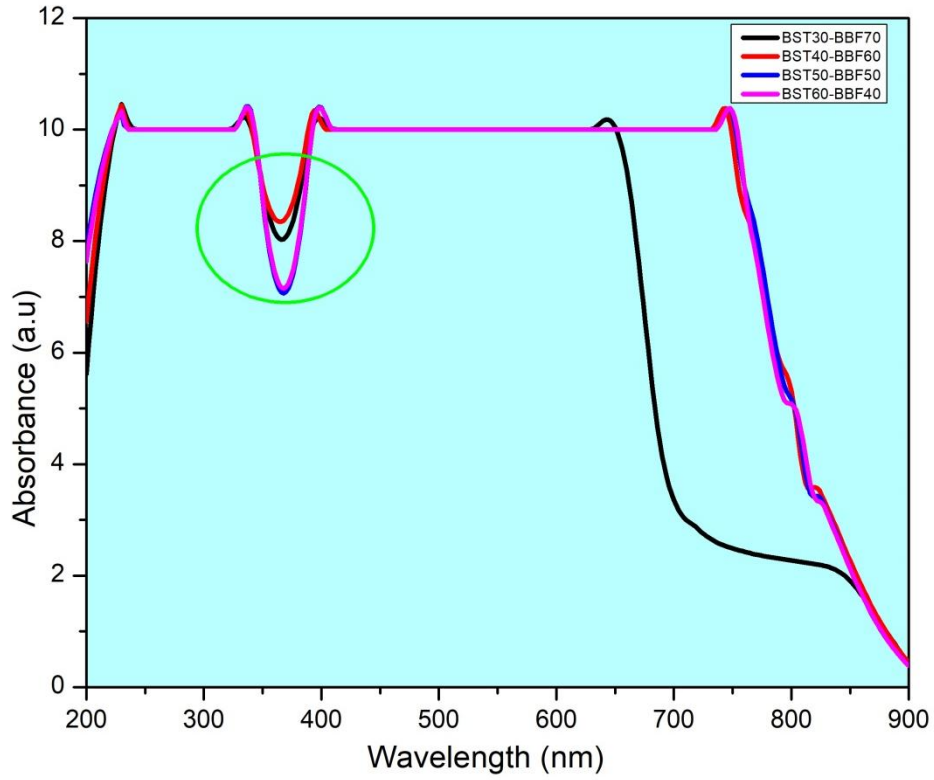

Fig 2 Optical absorption (A) vs wavelength for all the BST-BBF glass-matrix samples

The absorption coefficient α was calculated from the relation, based on Beer- Lamberts law:

$$\alpha = 2.303A/d \quad (2)$$

where d represents the sample thickness and A is the absorbance of the sample.
Optical energy band gap (E_{opt}) was calculated from Tauc relation given by Davis and Mott:

$$\alpha h\nu = B(h\nu - E_{opt})^{\gamma} \quad (3)$$

B is the band edge sharpness constant or proportionality constant which is associated with the type of electronic transitions and is independent of energy. The term hν represents the incident photon energy in eV. The variation of $(\alpha h\nu)^{\gamma}$ as a function of photon energy hν known as Tauc plot for $\gamma=1/2$ is shown in the Fig 3(a-d) for all the glass-matrix samples.

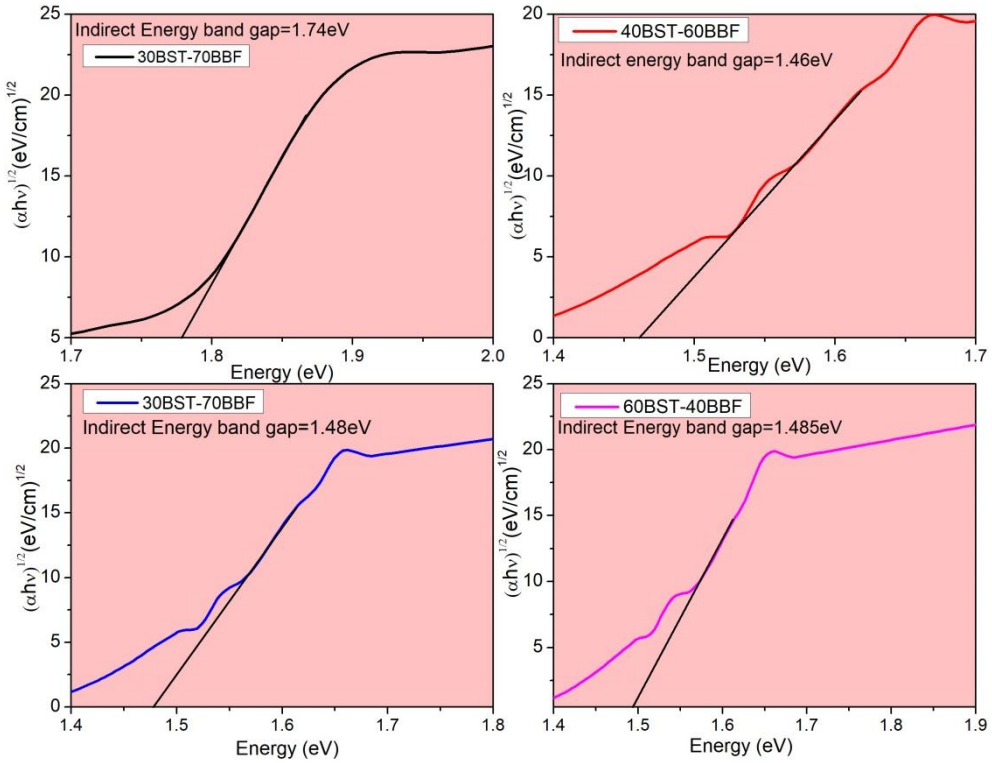

Fig 3 (a-d) $(\alpha h\nu)^{\gamma}$ vs. photon energy ($h\nu$) for all BST-BBF glass-ceramics

The optical energy band gap is evaluated by extrapolating the linear region of the graph (Fig 3) onto the x-axis of the Tauc plot where it has the zero absorption i.e $(\alpha h\nu)^{1/2} = 0$. Urbach energy quantifies the steepness of the onset of absorption near the band edge hence the broadness of the density of states and is the characteristics of the structural disorder and imperfections. From the values, given in Table 3, it is observed that with increasing the BST content in the glass ceramics, the Urbach energy reduced from 0.1eV to 0.06eV, owing to the fact of lower defect concentration in the localized states. The absorption coefficient is calculated from the Urbach energy, based on the following Eqn:

$$\alpha = \alpha_0 e^{\frac{h\nu - E_{opt}}{E_U}} \qquad (9)$$

Here α_0 is a constant, h is the Planck's constant, ν is the photon frequency, EU_{is} the Urbach energy and E_{opt} is the optical energy band gap. The above equation when reduced to a linear equation form, the inverse of the slope of the linear part of the graph between lnα and energy hυ gives the Urbach energy. The variation of In (□) with photon energy is shown graphically in the Fig 4.

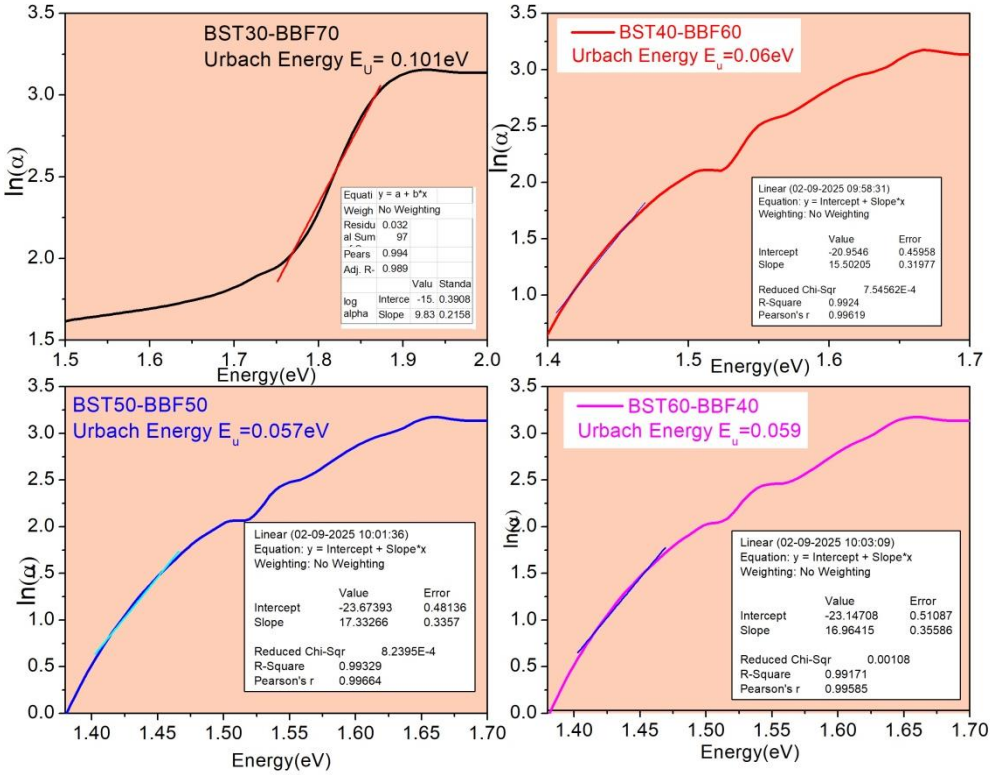

Fig 4: In (□) vs. photon energy (h□) for all the glass-matrix samples

The static refractive index of the all the samples are calculated from the relation between optical energy band gap and refractive index,

$$n = \sqrt{\frac{A}{E_g^{0.5}}} - B \qquad (4)$$

where A and B are constants and has its usual significance. The dielectric constant (ε), molar Refractive index $R_{m,}$ metallization criterion (M) and electronic polarizability (α_m) can be obtained using the following relations and the values were summarized in Table 4.

$$\varepsilon = n^2 \qquad (5)$$

$$R_m = (n^2 - 1/n^2 + 1) * V_m \qquad (6)$$

$$\alpha_m = \frac{3}{4\pi N} * R_m \qquad (7)$$

$$M = 1 - \left(\frac{R_m}{V_m}\right) \qquad (8)$$

Sample	Refractive index 'n'	Dielectric constant (ε)	Molar refractivity (R_m)(m^3/mol)	Metallization criterion (M)	Electronic polarizability(α_m) ($C.m^2.V^{-1}$)
BST30-BBF70	2.67	7.85	65.73	0.246	$2.61x10^{-23}$

BST40 -BBF60	2.82	7.95	71.96	0.223	$2.85x10^{-23}$
BST50-BBF50	2.81	7.89	81.82	0.224	$3.24x\ 10^{-23}$
BST60-BBF40	2..80	7.84	90.28	0.202	$3.58x\ 10^{-23}$

Table 4. Refractive index, dielectric constant, molar refractivity and metallization criterion values of all the glass-ceramic samples

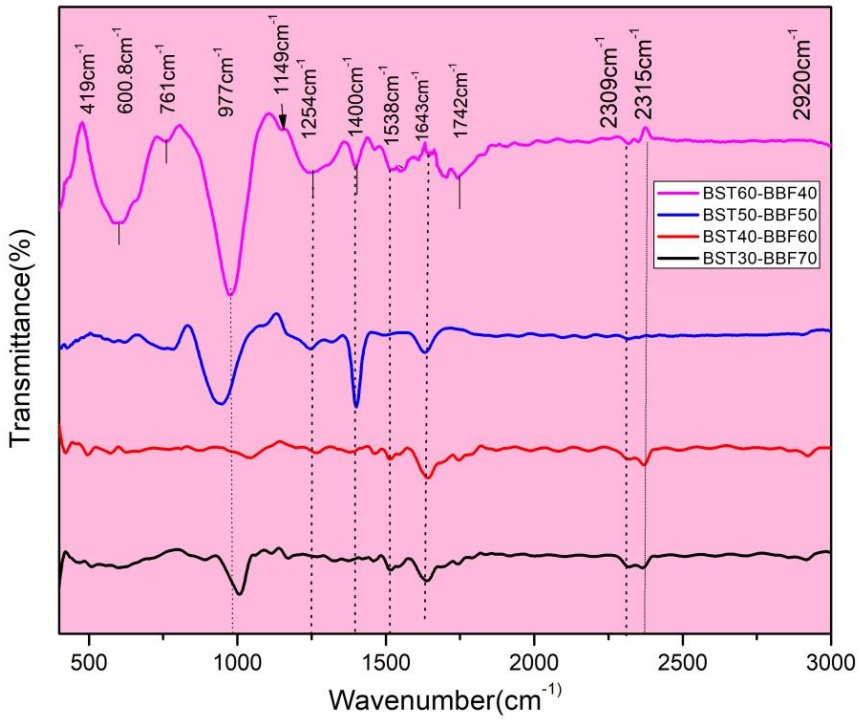

Fig 5 FTIR spectra for all the glass-ceramics

The FTIR transmission spectra of the glass-ceramics were recorded over the range of wavenumber 400cm^{-1} to 3000 cm^{-1} and shown in the Fig 5. The absorption bands reveal the ordering of the fundamental structural units. The obtained absorption bands explain the network forming and network modifying groups. As the mass of bismuth is more compared to boron, the vibrational modes of borate network are formed above 900 cm^{-1}. The transmission band peaked at 419 cm^{-1} refers to the vibrations of Bi-O and Bi-O-Bi in distorted BiO_6 units. The peak at 600 cm^{-1} and 761 cm^{-1}is ascribed to bending vibrations of B-O-B linkages of BO_3 units and Ti-O -Ti symmetric stretching vibrations of TiO_6 structural units. The peak at 977 cm^{-1} may be assigned to B-O stretching vibrations in BO_4 units from di-borate groups. The bands observed at 1149 cm^{-} and 1254 cm^{-1} can be assigned to the stretching vibrations in the BO_4 units from tri, tetra and penta borate groups and to the B-O stretching vibrations of trigonal BO_3 units. The peak at 1400 cm^{-1} could be assigned to B-O stretching modes of trigonal BO_3 units in orthoborate groups. The IR peaks observed near 1400 cm^{-1} can be assigned to the antisymmetric stretching vibrations with three non-bridging oxygens (NBO) of B-O-B groups. It should remember here that bismuth ions, acting as network modifiers or formers, can facilitate the formation of the mentioned above units, which contribute to different vibrational modes. More aspect of this would be discussed in the following Raman mode analysis.

Raman spectroscopic plot for all the samples, obtained at room temperature is as shown in the Fig6. The Raman modes observed are marked in the spectrum The peaks got broadened and the intensity also increased with the increase of BST composition and additional peaks centered at 572 cm^{-1} and 629 cm^{-1} are found for the highest composition of BST. Ram modes observed near 570 cm^{-1} of boro-bismuth glasses indicates the presence of B-O-B bending vibrations of borate ring [18,19]. However, these Raman bands may shift slightly depending upon the exact composition of the glass-network.

It is known fact that the boron can exist in both trigonal (BO_3) and tetrahedral (BO_4) units. The presence of both units and changes observed in the bands are due to the addition of bismuth oxide based martials namely BST in the glass-matrix. On account of bismuth, the bands can become either broaden or multiple

bands or splitting of existing bands. A splitting observed for higher concentration of BST-glass matrix (60BST-40BBF) is due to the changes in vibrational coupling or bond strengths. The formation of Bi-O-Bi bands are attributed to the high polarizing nature of Bi^{3+} ion, which can significantly alter the vibrational frequencies, and hence contributes the splitting observed in the Raman bands near 600 cm^{-1}. It is observed that layered-perovskite materials like BST undergo the structural phase transitions and that affect its Raman spectra. The transitions involve changes in its crystal structure can cause bands-split or may disappear with increasing the glass-matrix.

The Raman peak observed at 282 cm^{-1} for BST60-BBF40is attributed to the symmetric vibrations of Bi-O-Bi link. Two peaks observed in the region of 572 and 629 cm^{-1} can be ascribed to the Bi-O stretching vibrations of BiO_6 units. The peak at 755 cm^{-1} is due to the four coordinated Ti atoms in TiO4 units and six coordinated Ti atoms in TiO_6 structural units. Raman bands at high frequency (>1200cm-1) gives information of short range order in the borate glass system. These bands are related to tetrahedral borate groups or to the B-O stretching vibrations involving non-bridging oxygens.

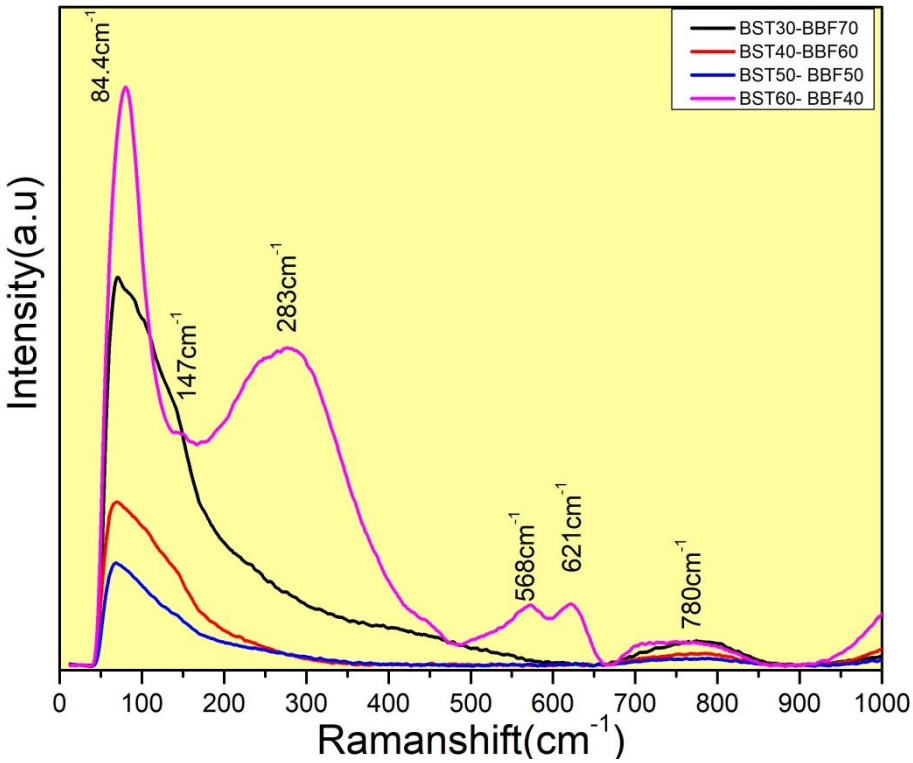

Fig 6 Raman spectrum for all the BBF-BST glass ceramics

Bismuth based perovskite glass ceramics free from lead and therefore they are growing as radiation shielding materials owing to their high density, dielectric property and enhanced optical properties. Borate glasses with heavy metal oxides of bismuth could increase the glass density, which in turn enhances their radiation shielding abilities [20]. The ionizing radiations interact with the shielding material acting as an attenuator through absorption of radiation. Radiation shielding capability of the present materials were studied in the present work. We have analyzed radiation parameters such as mass attenuation coefficient (MAC), N_{eff} (Effective electron density) and Z_{eff} (effective atomic number). Exposure built-up factor (EBF) and energy absorption build-up factor (EABF) were also obtained from the simulation software in the energy range of 0.015-15Mev.

The variation in mass attenuation coefficient (MAC) values with respect to the photon energy is shown in Fig 7. MAC explains the ability of a material to attenuates the radiation per unit mass. It depends not just on the radiated photon emery, atomic number and density of the material. As observed in Fig 7, MAC has very high values ($\sim$ 5000 gm/cm^2) in the lower energy range (0.01 -0.04 MeV). This indicates that the photon absorption process becomes dominant at this region. A kink observed in the plot (shown as inset Fig 7) signifies the absorption of gamma photons by K-shell electron of bismuth compounds.

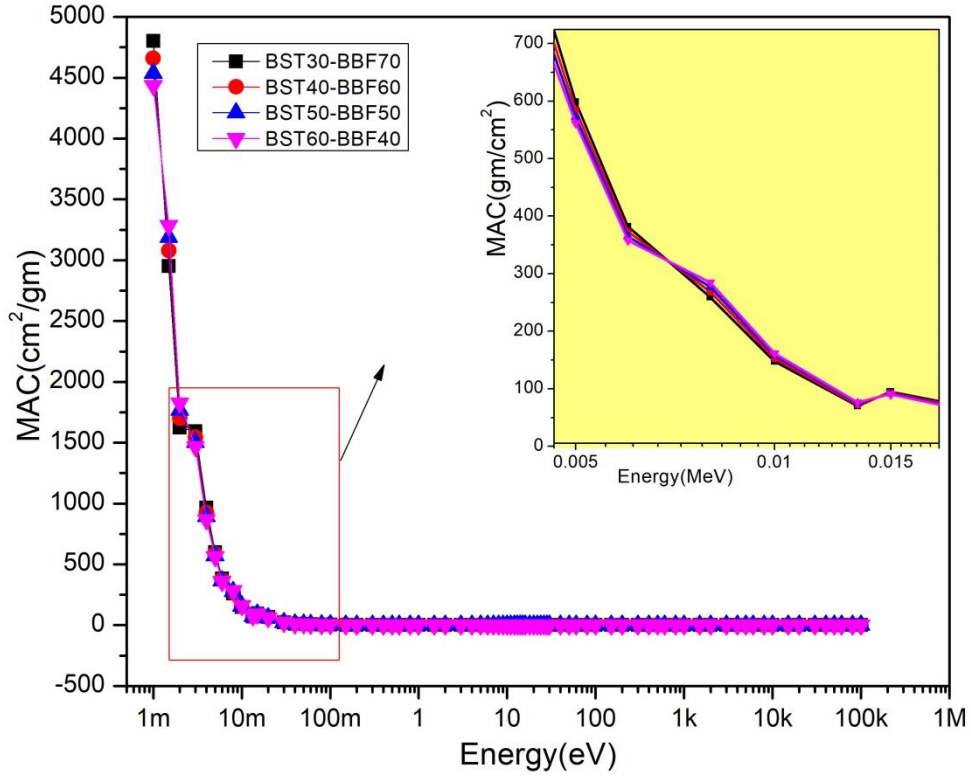

Fig 7. MAC vs energy (eV) for all BST-BBF glass ceramics: Inset Fig: Kink shown in the magnified region

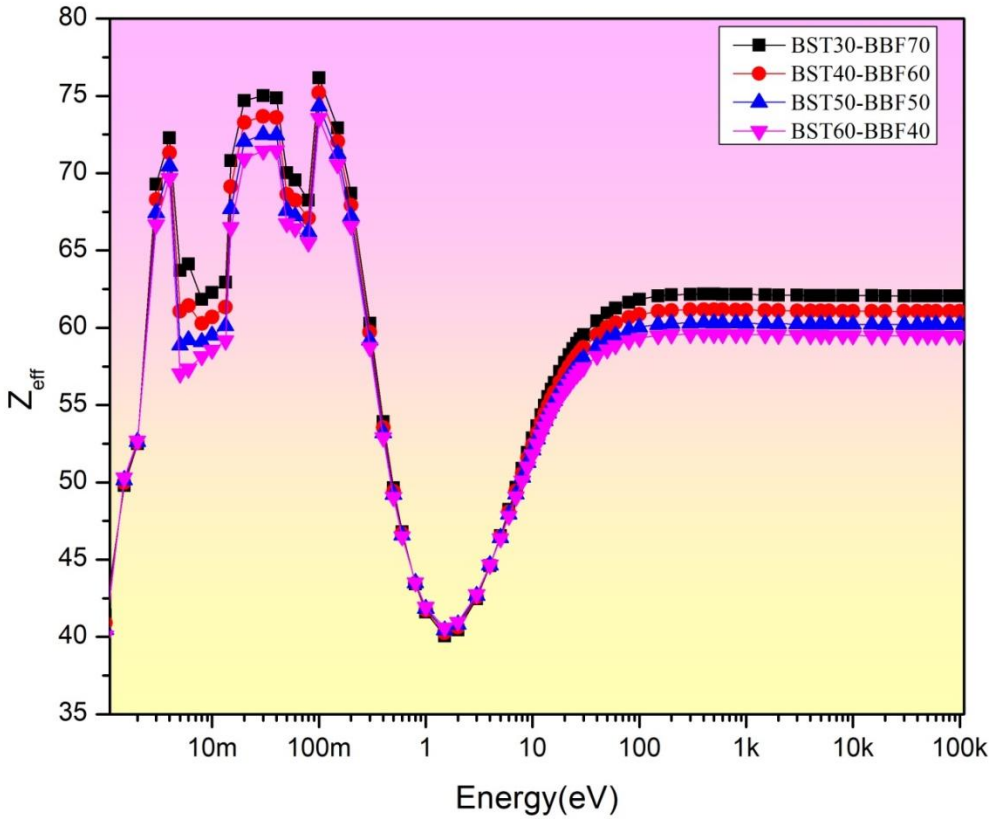

Fig 8. Effective atomic number (Z_{eff}) of BST-BBF glass ceramics as a function of gamma photon energy.

Fig. 8: shows the fluctuations in the effective atomic number (Z_{eff}) in the energy range of 0.015 to 200 MeV. Absorption peaks observed at low frequency region (marked as arrow) is attributed to photo absorption effect and at higher energy region, pair production plays a prominent role. The pair production is proportional to square of the atomic number. The multiple peaks observed in the region of 10-100 MeV (shown as double arrow) is due to the Compton scattering process [21]. The overall Z_{eff} for BST60-BBF40 is found to be less, compared to the other samples.

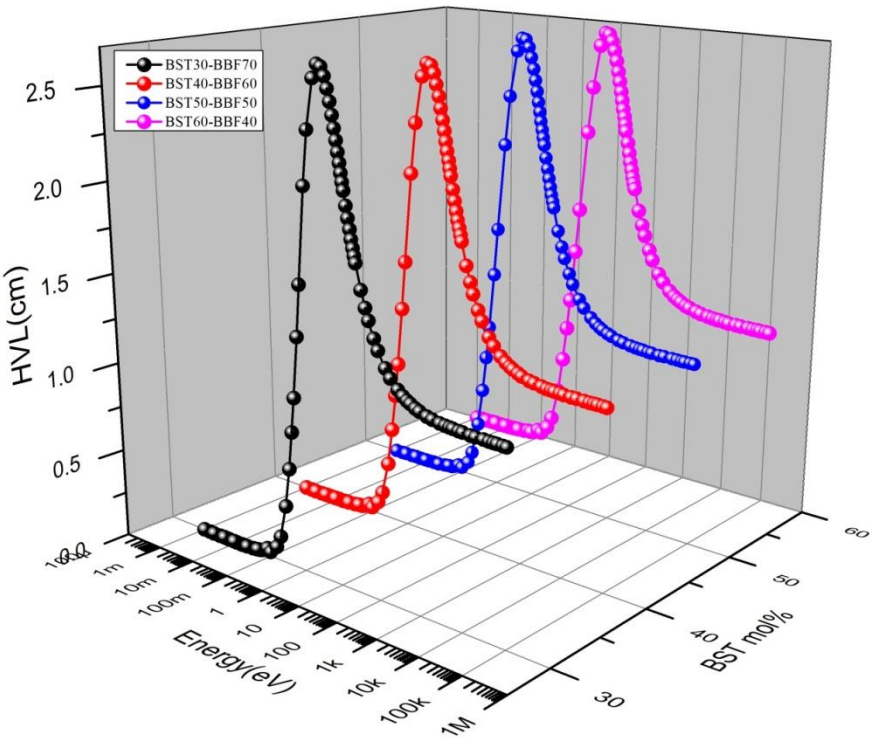

Fig 9. 3D plot of HVL and energy/BST composition of BST-BBF glass ceramics c

Fig 9 shows the change in the HVL (Half Value Layer) which is inversely related to linear attenuation coefficient in the energy range. From the plot it is evident that there is a slight change observed in the HVL values with the incorporation of BST in the glass matrix. From this it is evident the addition of BST on the glass matrix has shown impact in the absorption, as mentioned above.

The main two distinct features of buildup factors explain the ratio of total detector response of noncolloidal radiation. Energy absorption buildup factor (EABF) explains the amount of energy absorbed in the shielding material due to scattered photons and secondary particles. Whereas exposure buildup factor (EBF) explains the enhancement of radiation exposure in the air. Based on these factors one can build glass-materials to protect form the radiation. The variation of EABF and EBF with applied photon energy is shown in the Fig 10 and Fig 11 respectively.

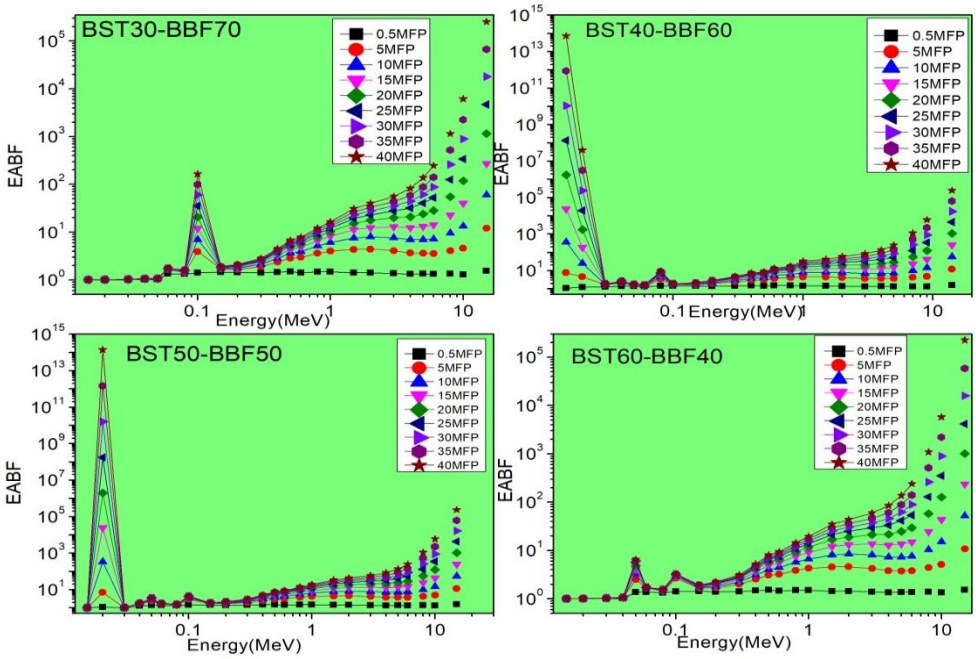

Fig 10 Variation EABF with photon energy for BST-BBF glass ceramics

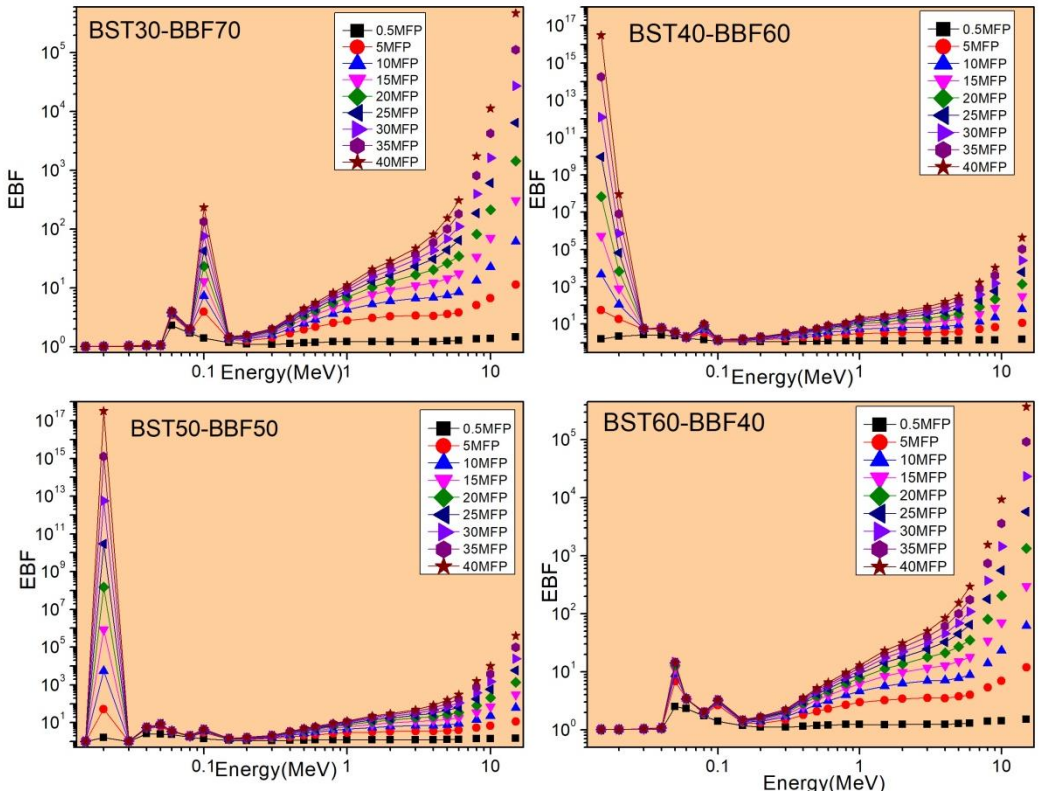

Fig 11. Variation of EBF with photon energy for BST-BBF glass ceramics

From the plots it is evident that both EABF and EBF were found to increase with increasing the photon energy. A sudden increase in EABF and EBF at lower energy region (> 0.1 MeV) indicates the Compton scattering is predominant process in lower energy region. Mean free path is the distance that a photon must travel before it gets absorbed or scattered by the shielding material. EABF and EBF are the critical factors which assess whether a material has good shielding ability or not. Generally low values of EBF and EABF are most desirable for better shielding property of the material. As projected in the above plots EBF and EABF increases with increasing photon energy. This is the essential characteristic feature fop Compton scattering process.

4. Conclusions

Glass matrix with of (100-x) [0.7Bi_2O_3-0.2B_2O_3-0.1Fe_2O_3] + x ($Bi_{3.75}Sm_{0.75}Ti_3O_{12}$) (with x=30, 40, 50, 60 wt.%), were prepared by conventional melt–quench method. From X-ray diffractogram it is revealed that crystalline phase becomes dominant with increasing the BST composition. The glass-sample have shown a shift in cutoff wavelength near 815 nm. The optical energy band gap values were found to decrees with increasing the BST composition. This could be due to the lowering of conduction band through localized energy levels in the band gap or could be because of modulation of orbital overlap and compensation mechanism. The samples were found to be opaque in nature and absorbed almost all the radiation in the UV-VIS light. This kind of remarkable characteristic feature is needed for future photovoltaic applications. A shift in the 1000 cm^{-1} absorption peak is a direct indicator of structural rearrangements in the boron-oxygen framework of bismuth glasses. The splitting of Raman band at ~572 and ~620 cm^{-1} suggests a complex-interplay of structural changes within the bismuth borate glass network. The same can be ascribed to the bending vibrations within the TiO_6 octahedral of layered perovskite structure. This is considered to be a key component of layered-perovskite structure. From gamma ray shielding parameters, 60BST-40BBF has shown lower values for both EBF and EABF. From this it is concluded that this glass ceramic is a good radiation shielding material. However, at higher energy regions buildup factor values were found to high due to multiple scattering process. Based on the sudden change in buildup factor value at very low photon energy, these materials can be used as shielding materials in nuclear technology.

Acknowledgements: Authors thank Late Prof. Syed Rahman sir for his early insights and encouragement during initial stages of this research work and directly influenced the fundamental structure and design of the research problem.

REFERENCES:

[1] A. Tumarkin, N. Tyurnina, N. Mukhin, Z. Tyurnina, O. Sinelshchikova, A. Gagarin, E. Sapego, Y. Kretse, Composite Structures **281** (2022) 114992.
[2] G. Singh, M. Sharma, R. Vaish, Communications Materials **1** (2020) 100.
[3] M.H.A. Mhareb, M.I. Sayyed, N. Alonizan, M.A. Almessiere, I. Baig, et al., Nuclear Engineering and Technology **56** (2024) 4708–4715.
[4] A. Kumar, A. Jain, M.I. Sayyed, F. Laariedh, K.A. Mahmoud, et al., Scientific Reports **11** (2021) 7784.
[5] A. Madhu, S.-A. Idris, N.S. Abd El-Gawaad, V.B. Tangod, N. Srinatha, Journal of Molecular Structure **1294** (2023) 1136445.
[6] A.Z. Khalf, Ferroelectric Glass-Ceramic Systems for Energy Storage Applications, IntechOpen (2020). https://doi.org/10.5772/intechopen.93855
[7] M.P.F. Graça, M.A. Valente, MRS Bulletin **42** (2017) 213–219.
[8] C. Porwal, G. Singh, M. Sharma, V.S. Chauhan, et al., Progress in Solid State Chemistry **77** (2025) 100497.
[9] M.-J. Pan, M. Lanagan, B.A. Bender, C.-T. Cheng, in: W. Wong-Ng, A. Goyal, R. Guo, A.S. Bhalla (Eds.), High Energy Density Ferroelectric Glass-Ceramics, Wiley, 2006, 437–464. https://doi.org/10.1002/9781118408476.ch18
[10] M.C. Gonçalves, L.F. Santos, R.M. Almeida, Comptes Rendus Chimie **5** (2002) 845–854.
[11] M.H.M. Zaid, H.A.A. Sidek, K.A. Matori, A. Abdu, K.A. Mahmoud, M.M. Al-Shammari, E. Lacomme, M.A. Imheidat, M.I. Sayyed, Journal of Materials Research and Technology **11** (2021) 1322–1330.
[12] A. Kumar, A. Jain, M.I. Sayyed, F. Laariedh, K.A. Mahmoud, et al., Scientific Reports **11** (2021) 7784.
[13] N.V. Prasad, S.N. Babu, A. Siddeshwar, G. Prasad, G.S. Kumar, Ceramics International **35** (2009) 1057–1062.
[14] E.V. Ramana, N.V. Prasad, D.M. Tobaldi, J. Zavašnik, M.K. Singh, et al., RSC Advances **7** (2017) 9680–9692.
[15] G.A. Khater, B.S. Nabawy, J. Kang, et al., Silicon **12** (2020) 2921–2940. https://doi.org/10.1007/s12633-020-00391-8
[16] S. Dubuis, S.H. Messaddeq, Y. Ledemi, A. Côté, Y. Messaddeq, Optical Materials Express **11** (2021) 2560.
[17] R.K. Mishra, S.K. Avinashi, S. Kumari, S.R. Nain, T. Katheriya, R.K. Dwivedi, S. Upadhyay, C. Gautam, Journal of Alloys and Compounds **990** (2024) 174354.
[18] B. Srinivas, K.M. Katubi, A. Bhogi, et al., Optical and Quantum Electronics **56** (2024) 784. https://doi.org/10.1007/s11082-024-06596-0
[19] K. Serkina, I. Stepanova, A. Pynenkov, M. Uslamina, K. Nishchev, K. Boldyrev, R. Avetisov, I. Avetissov, Ceramics **6** (2023) 1559–1572. https://doi.org/10.3390/ceramics6030097
[20] Z.A. Alrowaili, E. Yılmaz, F. Çalışkan, B. Öztürk, I.O. Olarinoye, H. Arslan, Radiation Physics and Chemistry **204** (2023) 110711.
[21] S.B. Kolavekar, G.B. Hiremath, P.N. Patil, N.M. Badiger, N.H. Ayachit, Heliyon **8** (2022) e11788.